Supercomplex wave-vortex multiscale phenomena induced in laser-matter interactions

S. Lugomer
Material Physics Department, "Ruđer Bošković" Institute, Bijenička c.54, 10001 Zagreb, Croatia

Y. Fukumoto
Graduate School of Mathematics, Kyushu University 33, Fukuoka 812-8581, Japan

B. Farkas
Department of Optics and Quantum Electronics, University of Szeged, P.O. Box 406, H-6701 Szeged, Hungary

T. Szörényi
Research Group on Laser Physics of the Hungarian Academy of Sciences, University of Szeged, P.O. Box 406, H-6701 Szeged, Hungary

A. Toth
Research Institute for Technical Physics and Material Sciences, Hungarian Academy of Sciences, P.O. Box 49, H-1525 Budapest, Hungary

(Received 6 September 2006; revised manuscript received 4 April 2007; published 12 July 2007)

The interaction of laser light with a metal surface yields a complex configuration of point defects, e.g., droplets and holes and vortex microfilaments. When a single filament interacts with a defect it "winds" around the defect and can form loops, and rings. Interaction of a single filament with a single defect gives rise to arc deformation bending, formation of loops and rings, while its interaction with a two-dimensional (2D) random lattice of defects gives rise to the vortex filament splitting and breaking which occur at nodal points of the Voronoi lattice. Interaction of one-dimensional (1D) vortex filament lattice with 2D lattice of defects results in the formation of knotted structures such as the Hopf links as well as 1D and 2D Hopf link crystals, knotted along the sides of the Voronoi lattice. We observed that configurations of vortex filaments are organized at three hierarchical levels of growing complexity. Every level is comprised of the elements of the lower complexity one, indicating the presence of a supercomplexity.

DOI: 10.1103/PhysRevE.76.016305 PACS number(s): 47.20.−k, 47.61.−k, 47.80.Jk, 47.32.C−

I. INTRODUCTION

Nanosecond laser-matter interactions (LMI) on a solid surface may generate Rayleigh-Taylor/Richtmyer-Meskhow (RT/RM) accelerated *inhomogeneous flow environments* where wavylike structures appear on the molten surface [1–6]. Depending on the laser parameters, the material parameters and the experimental conditions, the surface waves may range from shallow small-amplitude and small-wavelength capillary waves to deep nonlinear waves [7]. The evolution of nonlinear waves may lead either to the formation of vortex microtubes (vortex filaments), or to the formation of breaking waves giving rise to very complex wave-vortex (WV) scenario.

Vortex filaments, generated in the RT environment by the Kelvin-Helmholtz instability of the shear layer, appear as corotating vortex tubes with the same circulation polarity: C+C+C+. In the RM environment, they are generated by the baroclinic instability and vorticity deposition, and appear as counter-rotating vortex tubes with alternating circulation polarity: -C+C-C+C–[8,9]. In a heuristic simulation the accelerated flows that form coherent vortex structures in laser generated RT and RM environments under various laser and material parameters were briefly reported by Zabusky, Lugomer and Zhang [6]. This has initiated an in depth study on the generation of vortex filaments from vorticity deposition, formation of vortex filament rolls, vortex filament helical pairing, reconnection and merging (Lugomer [7]). An intriguing phenomenon observed in this series of studies is the interaction of individual vortex filaments or a one-dimensional (1D) vortex filament lattice with point defects such as droplets and bubbles which result in a number of complex configurations that in the context of LMI were not previously discussed.

The aim of this study is to provide experimental evidence for the generation of complex filamentary structures in close interaction with point defects and to shed more light on their characteristics. We show in this paper that laser-generated surface wave-vortex structures span the spatial scale from nanometers to micrometers, and approaching the millimeter scale establishes the scenario for a multiscale phenomena. In close interaction with point defects such as rigid spheres and holes (exploded soft spheres or bubbles), vortex filaments give rise to complex configurations. Among them are the looping of vortex filament around a rigid sphere which can be interpreted on the basis of the Pedrizzetti model [10], spiraling of filament around point defect in agreement with Fukumoto [11], and pinning which can be interpreted on the basis of the Schwartz model of pinning at protrusion [12]. In addition, the individual and collective pinning of filaments at a hole in the presence of weak and strong shear, have also been observed. Pinning of filaments at material defects is well known to occur in various physical, chemical, and biological systems. Vortex filaments or stringlike structures are pinned to the defects in various systems, an example of which is pinning of the magnetic flux strings in hard type II

superconductors Blatter *et al.* [13] and Tonomura *et al.* [14], of carbon nanotubes to defects on silicon substrate [15], of spiral waves in excitable media [16], of various biological strings [17] ranging to the pinning of DNA molecules on various substrates [18]. When completing the list with recently observed pinning of magnetic flux filaments in the Sun's penumbra [19,20], one can say that pinning is a common phenomenon taking place in the filamentary organized matter from the atomic to the astrophysical scales. While pinning of magnetic flux strings in superconductors can be visualized with a field emission electron microscope [14], in LMI the strings of vortex filaments on the surface are observed by scanning-electron microscope (SEM) micrographs of residual structures. The SEM analysis shows that the organization of laser-generated vortex filaments both at a single pinning center and at a random array of pinning centers is more complex than observed in other systems. The variety of vortex filament configurations in the trapping regions of defects include the single-filament arc-bending, as well as the formation of loops and vortex rings, associated with filament splitting and/or breaking. Configurations resulting from the interaction of a 1D vortex filament lattice and a 2D random field of defects range from the pair of knotted rings (Hopf links) to the 1D and 2D Hopf-link crystals. The organizational complexity of these structures when classified at more than one hierarchical level, exhibits some common configuration elements, which indicates the presence of supercomplexity.

II. EXPERIMENT

A series of experiments was performed on indium plates in the *semiconfined* configuration (SCC). Here, the target surface is irradiated from above through a transparent quartz plate positioned ~300 μm above the surface. Laser ablation and plasma evolution occurs in a confined channel-like trap due to the reflection of the upward propagating plasma shock wave which enhances the horizontal plasma expansion and promotes the formation of a plasma slab [Figs. 1(a)–1(c)]. This plasma bubble accelerates horizontally over the melted surface layer of indium and yields the formation of a RT/RM environment. Finally, these environments support the formation of nonlinear waves which evolve into coherent structures of the vortex filament type.

In the first series of experiments, an In plate of ~0.3 mm thickness has been irradiated by single pulse of a KrF excimer laser (wavelength: $\lambda=248$ nm; pulse duration: $\tau=20$ ns), in the semiconfined configuration (SCC), while the laser energy was varied from 73 mJ to 100 mJ.

Another series of experiments has been performed by means of a XeCl excimer laser ($\lambda=308$ nm, $\tau=20$ ns, $E=100$ mJ) on Co-coated steel using 14 consecutive pulses. In all cases the temporal shape of the pulses was Gaussian and the lateral intensity distribution was Gaussian along the shorter axis of the rectangular beam. The surface temperature of the film is estimated on the basis of the relation [21]

$$T(z=0,t)=\frac{2I}{\sqrt{k\pi}}\sqrt{\alpha t}, \tag{1}$$

where t is the time, k is the thermal conductivity (81.8 J/msK for indium), α is the thermal diffusivity (assumed to be 0.1 $cm^2/s=10^{-5}$ m^2/s), and I denotes the laser intensity. The temperature of the surface layer was determined for $I=7\times10^7$ W/cm^2 which corresponds to $E=100$ mJ, spot size $S=6.8\times10^{-2}$ cm^2, and $t=10$ ns (i.e., for $\tau/2$ which is the time when the pulse is at maximum, and the time when the cooling phase begins). The Gaussian power distribution in the y direction generates a flatlike temperature distribution as shown in the upper diagram in Fig. 2(a). Calculation gives the temperature in the center $T_0=2964$ K, while at the distance of ~1.3 mm in the $+y$ and $-y$ directions away from the centerline, it is still $\sim0.8T_0$, i.e., about ~2371 K. This gives the symmetric temperature difference of $\Delta T_y=593$ K from the hot centerline in the y direction, which corresponds to a gradient of $\nabla T_y=\Delta T_y/(L_y/2)=456$ K/mm. The melting point and the boiling point of indium is 429 K and $T_b=2375$ K, respectively. Because the maximum temperature, i.e., $T_0=2964$ K is higher than the

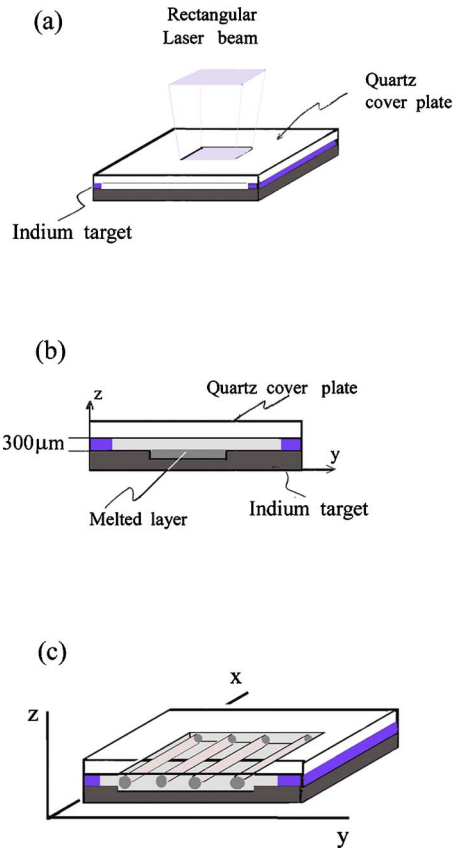

FIG. 1. (Color online) Laser-matter interaction (LMI) in the semiconfined configuration (SCC). (a) The rectangular laser beam illuminates indium surface through transparent quartz coverplate positioned about 300 μm above the target surface. (b) Laser ablation causes the formation of a plasma layer above the melted indium surface [cross section in the (x,y) plain]. (c) Laser plasma evolution occurs in a channel-like trap so that plasma shock wave is reflected back to the surface. Subsequent formation of a plasma slab causes horizontal acceleration of the melted indium layer and leads to the formation of the Rayleigh-Taylor or the Richtmyer-Meskhow (RT/RM) environment. The RT/RM environment supports the formation of nonlinear waves which evolve into coherent structures of the vortex filament type (schematically).

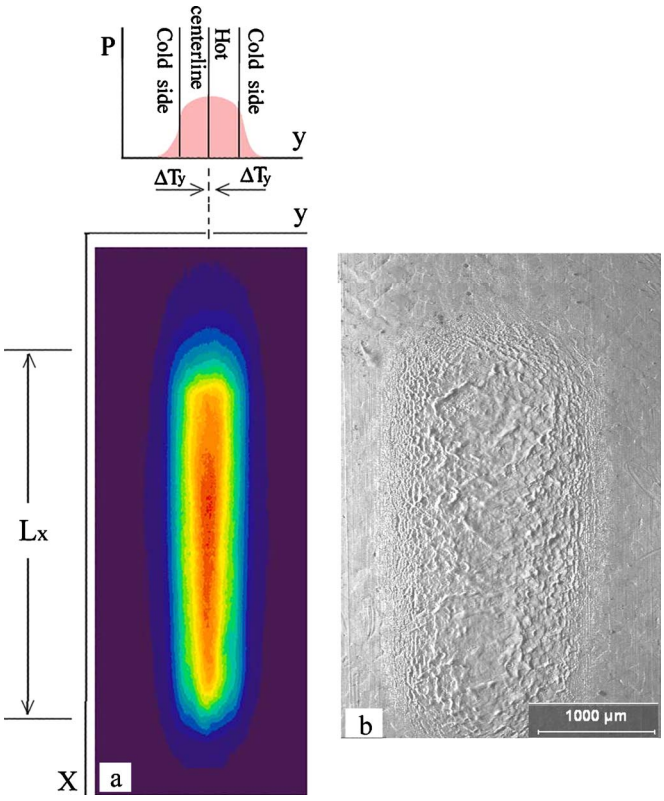

FIG. 2. (Color online) Intensity distribution of the KrF laser across the liquid cell. (a) The Gaussian laser power distribution along the y axis causes similar temperature distribution across the spot. (See schematic diagram at the top.) (b) The flat-top (or super-Gaussian) laser power distribution along the x axis causes an almost constant temperature distribution along the spot. Such distribution is the origin of a hot centerline along the cell, which establishes two symmetric cold sides. (b) Micrograph of the irradiated In target surface (low magnification).

boiling point of In, the liquid layer in the central region is in the metastable phase (superheated).

The generation of vortex filaments in RT/RM environments is promoted by the surface scratches which form the origin of perturbation for the accelerated fluid layer at the low-density–high-density interface. Therefore, a series of parallel micron size scratches, collinear with the longer axis of the rectangular laser beam was used to assist in the formation of a quasiregular 1D vortex filament lattice (because filaments are not strictly equidistant). The distance from the center of the laser irradiation spot affects the degree of roll up and the motion of the filaments and behavior of resulting features frozen into different domains of the spot.

While the origin of the vortex filaments is in the nonlinear dynamics of the accelerated fluid in the RT/RM environment, the origin of the point defects is the instability of the metastable (superheated) phase of the liquid surface layer characteristic to the semiconfined configuration of LMI. Point defects, especially droplets are generated either as individual microdroplets or random arrays of defects/droplets behind the moving triple contact line of superheated fluid [22,23]. If superheating is low or absent, holes may be generated by random nucleation of bubbles and their explosion when the bubble reaches the critical radius [22]. Both cases may be present in LMIs, depending on the boiling point (T_b) of the material, the type of laser, and the experimental conditions. Holes may also be generated during the interaction of vortex filaments with a bubble because the bubble explode when a filament touches it. The bubble explosion may generate a hole with or without a vortex ring at the rim.

By the end of the pulse, the pattern of structures, formed by the interaction of vortex filaments with point defects in the melted metal layer, is frozen ultrafast at the rate of $\sim 10^9$ K/s, which preserves the complex configurations and makes their *a posteriori* analysis possible [Fig. 2(b)].

III. RESULTS AND DISCUSSION

A. Generation of vortex filaments

Laser irradiation of a metal target, patterned with a series of parallel micron size scratches, collinear with the longer axis of the laser beam, causes the formation of a 1D vortex filament lattice such as the one formed in melted surface layer of indium (Fig. 3).

Parallel scratches (along the x direction) cause the transversal perturbation of the shock wave as $\Psi = A \exp k_p y$ (A is the amplitude of the perturbation equivalent to the height of the scratch wall, and k_p is the wave vector of the perturbation, $k_p = 2\pi/L$, where L is the scratch-to-scratch distance). An oscillating shock which perturbs the interface transversely to the radial flow (y direction), causes the rollup into vortex tubes [20] so that a 1D vortex filament lattice has been formed. In LMI the ordering of vortex filaments, induced by the parallel scratches on target surface is similar to the ordering of carbon nanotubes induced by alternating parallel set of hydrophilic and hydrophobic surface stripes [15].

On the basis of estimating the parameters of the shear layer according to Fukumoto and Lugomer [20], we assume that the fluid velocity, U is approximately $U \sim 5000-6000$ m/s, the kinematic viscosity, ν is about 10^{-4} m^2/s to 10^{-5} m^2/s, and the Reynolds number $\mathrm{Re} = hU/\nu$ is $\mathrm{Re} \sim 10^3$ to 10^4, what we actually found to be about 3×10^3 [24,25]. The size of defects is in the range of $\sim 5-30$ μm, while the core size of vortex filaments is $\sigma \sim 3.5-7$ μm and their length is $\sim 1000-3000$ μm, so that they may be assumed as being infinite in length. The vorticity $\omega = \mathrm{rot}\ U$ and the circulation Γ is $\Gamma = 2\pi\sigma U \sim 0.26$ m^2/s [24].

The interaction of individual and collective vortex filaments organized into 1D lattice with point defects gives rise to various complex multiscale wave-vortex structures which capture physical phenomena on a very broad spatial scale. These structures establish an inhomogeneous pattern of vortex filament configurations in various domains of the interaction zone.

B. Trapping of vortex filaments at point defects

The simplest configuration emerges from close interaction of a vortex filament with a point defect which behaves like a trapping center. Trapping of vortex filaments can be described by the trapping potential V_t, originating from the

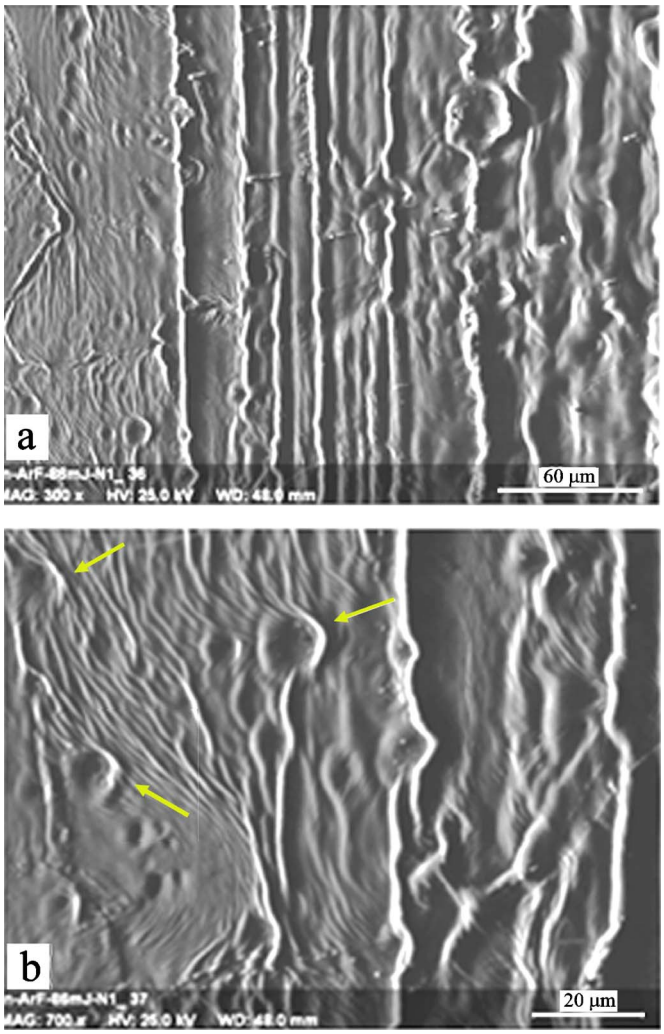

FIG. 3. (Color online) SEM micrograph of an In surface showing vortex filaments generated by KrF laser in SCC. (E=86 mJ). (a) Set of parallel vortex filaments (not strictly equidistant) which makes a quasi-one-dimensional vortex filament (1D VF) lattice. (b) Interaction of vortex filaments with point defects (holes) is marked by the arrows.

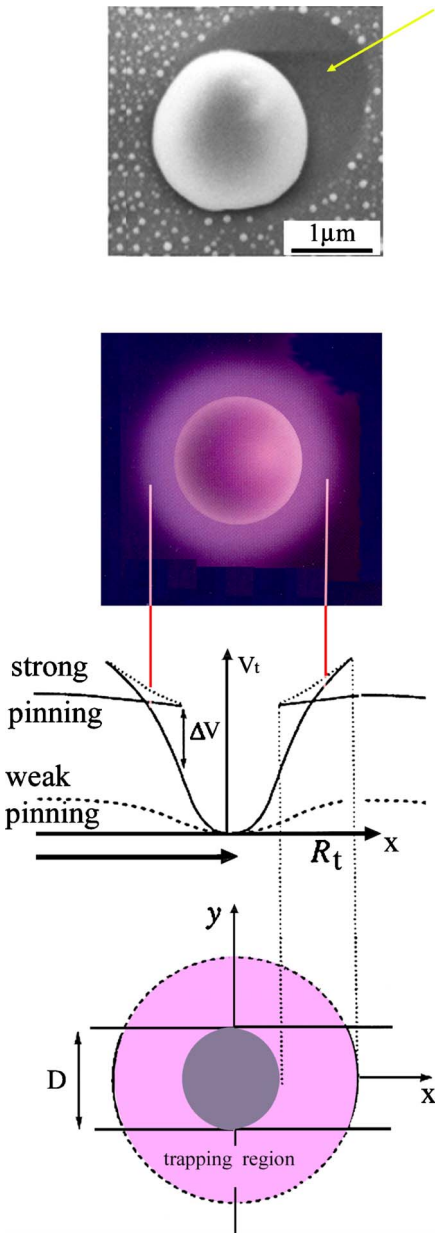

FIG. 4. (Color online) Trapping of a filament at a point defect (rigid sphere). The upper SEM micrograph shows a spherical droplet of indium. The SEM micrographs usually do not indicate the trace of the droplet (sphere) motion, indicating that they are stationary. However, on this particular image the empty space (trace marked by the arrow) at the top micrograph was made by the motion of a droplet for about 0.8 μm. The length of the trace of a droplet motion is much smaller than the core size of the vortex filament (~5 to 7 μm), and very small in comparison with the filament loop diameter (~10 to 50 μm). Therefore, it can be assumed that the sphere is a stationary or quasistationary one. The central picture is a dark sphere representing a point defect surrounded by a light shell (trapping region) of radius R_t. Trapping of the filament is caused by the potential V_t. The trapping force is $F_t = -\partial / \partial x\ (V_t)$, where $V_t \propto \Delta p$ and Δp is the pressure difference between the point defect and the surrounding area; corresponding trapping potential V_t and the effect of the trapping force on the filament configuration as a kind of landscape is schematically shown in the lower picture diagram.

pressure difference when the filament is in the close vicinity of a defect either because of self-induction, or because of shear flow. An analogy can be established between the trapping of vortex filaments at molten metal and the trapping of magnetic vortex filaments at point defects [13]. While the pressure difference or the hydromechanical force is responsible for trapping in the first case, it is the Lorentz force that is responsible for trapping in the second one [13]. Trapping of the filaments occurs at distances $R \leqslant R_t$, where R_t is the trapping radius (Fig. 4). The topmost panel of Fig. 4 shows the SEM micrograph of a spherical droplet of indium (point defect); the central picture is a sphere showing the point defect surrounded by the light spherical shell that represents the trapping region of radius R_t (interaction region). Trapping of the filament is caused by the trapping potential V_t as schematically shown in Fig. 4. The trapping (drag) force is $F_t = -\partial / \partial x\ (V_t)$, where $V_t \propto \Delta p$; Δp is the pressure difference between the point defect and the surrounding area. The trap-

ping potential V_t and the effect of the force on the filament configuration as a kind of landscape [13] is schematically shown in the lower picture diagram. Characteristics of the point defect, the vortex filament and the force field jointly determine the configurations of filament trapping, which include simple vortex filament looping, spiraling, and pinning at protrusions, as well as more complex configurations arising from interaction of 1D vortex filament lattice and 2D lattice of defects.

1. Trapping of filament at the rigid sphere by the looping process

A vortex filament that enters the interaction region of a droplet becomes trapped in its force field by the looping process [Fig. 5(a)(i)]. When approaching the sphere, the vortex filament first aligns itself along the circumference in a straight form; then, closer to the sphere it becomes arc bended aligning itself along its surface. Finally, at very small distances, the filament is turned backwards and the arc-bended segment transforms into a loop. A significant portion of the backward bent filament is in close contact with the straight, unbent portion; it could even wind one, two, or more times around it.

This process is analogous to the one that emerges from the Biot-Savart self-induction law as discovered numerically by Pedrizzetti [10]. A portion of the infinite vortex filament, close to the spherical droplet is perturbed by the image vortex and the portion, which is endowed with curvature, moves towards the surface by self-induction [10,26]. An image vortex system was necessary to be defined in order to obtain zero normal velocity of the fluid on the surface of the sphere. When approaching the surface the filament becomes strongly deformed as shown by analytical computation in the linear approximation [10]. In this idealized case of inviscid flow, vortex filament gets so close to a sphere that the finite core of the tube touches the surface of the sphere [10,26]. Then, it rapidly moves around the surface and forms a loop as really seen in the SEM micrograph in Fig. 5(a)(i). The schematic reconstruction in Fig. 5(a)(ii) gives an insight into this particular step of trapping: Dark circular center represents the core of the point defect, while the light circular region denotes the transitional zone from deformation to trapping.

The interaction of a vortex filament with a rigid sphere which results in the formation of vortex ring [Fig. 5(b)(i)], can also be understood using the numerical predictions of Pedrizzetti [10], for the case of an ideal inviscid flow. The vortex filament that starts to move around the rigid sphere creates a nonzero curvature and then the self-induced velocity leads it toward the body surface. Arriving very close to the surface the vortex filament rapidly stretches over the sphere and creates two opposite symmetrical kinks which eventually touch each other to give rise to a (stretched) vortex ring [10]. The formation of a vortex ring in the vicinity of a sphere is in agreement with the above given description [Fig. 5(b)(i)], and proceeds from the starting to the final configuration as shown schematically in Figs. 5(b)(ii) and (iii), respectively.

2. Trapping of filament at the hollow sphere by the looping process

When a vortex filament approaches a bubble (i.e. a hollow sphere) with a finite speed it is influenced by a distributed

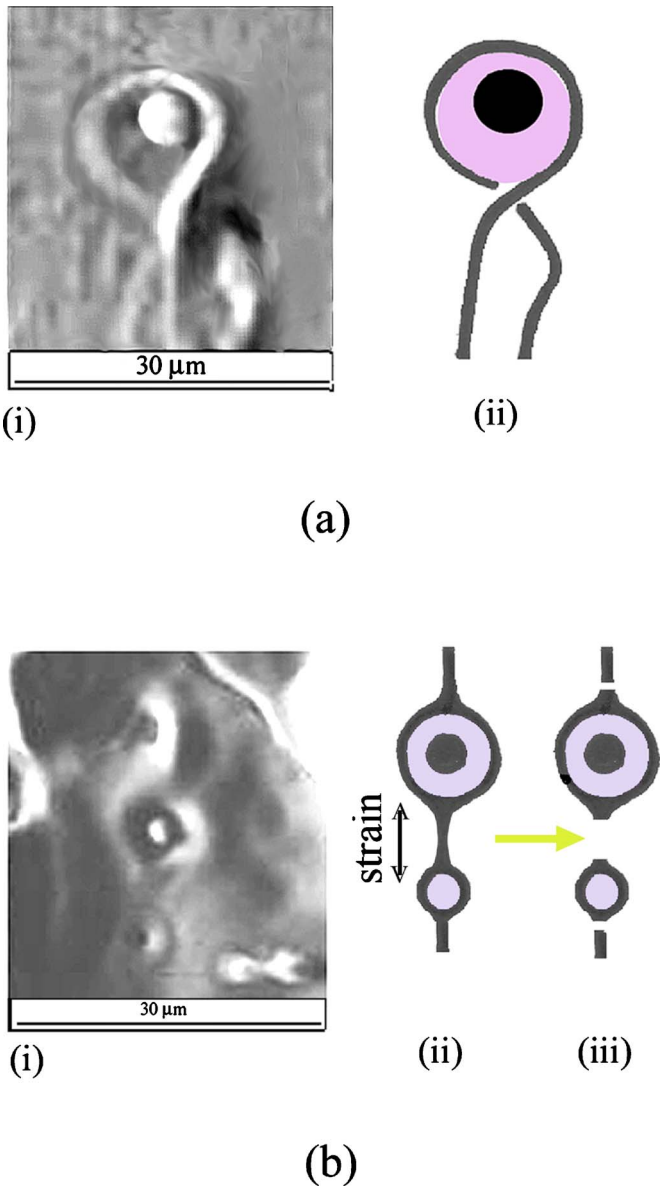

FIG. 5. (Color online) Close interaction of a vortex filament with a rigid sphere (E=86 mJ). (a) Looping of individual vortex filament around a rigid sphere. (i) SEM micrograph showing looping process; (ii) schematic illustration of the looping process shown in (i). (b) Formation of a vortex ring in close interaction of vortex filament with a rigid sphere (E=86 mJ). (i) SEM micrograph of vortex filament interaction with a hole defect that forms a vortex ring (E=86 mJ). (ii) Schematic representation of the looping process corresponding to (i). The vortex filament approaching a sphere becomes splitted into two filaments which bypass a droplet from the left and the right side. They reconnect at the opposite side of a droplet into a large filament, and then split again when bypassing the smaller hole defect. (iii) Stretching of a filament becomes very large and eventually causes the breakage of the filament at the points of largest strain.

vorticity on the interface, which is created to meet the stress continuity condition [27]. The interface vorticity becomes stronger as the curvature of the surface increases. But, generally, it is weaker than both the vorticity in the boundary layer on the surface of a rigid sphere and the image vorticity

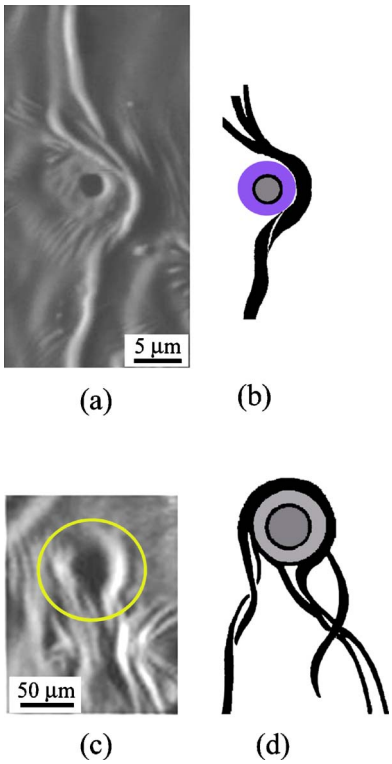

FIG. 6. (Color online) SEM micrograph of the VF arc-bending and looping at a hole (defect) (E=86 mJ). (a) VF after passing through the deformation zone of the hole/pinning center, becomes bended into semicircular arc and gets splitted at some distance from the hole. (b) Schematic representation of the VF configuration in the vicinity of a pinning center shown in (a). (c) Looping of VF at a hole defect followed by filament splitting at some distance from the hole. (d) Schematic representation of the VF looping shown in (c).

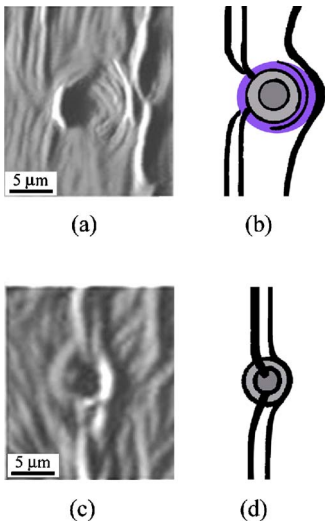

FIG. 7. (Color online) Complex interaction of individual vortex filaments with a hole (defect) (E=86 mJ). (a) SEM micrograph showing the VF configuration in the vicinity of a hole defect. The filament which comes very close to the hole becomes trapped (pinned) to the hole (left-hand side), while the filament at larger distance enters the deformation zone of the hole and becomes arc-bended (right-hand side). (b) Schematic representation of the filament configuration shown in (a). (c) SEM micrograph showing the pinning of VF that traverses the hole and appears at the opposite side. VF at the right-hand side is only arc-bended just like the one shown in (a). (d) Schematic representation of VF configuration sown in (c).

replacing the rigid sphere. The bubble explodes when the filament touches it and generates a hemispherical hole. The vortex filament interacts with the hole and makes a semicircular arc around it, as can be seen in Figs. 6(a) and 6(b). The looping process around a hole occurs via continuous bending similar to the spiraling of an elastic rod [Fig. 6(d)]. This process is associated with the vortex filament splitting because of the strong strain field surrounding the hole. The interaction between a set of vortex filaments and a hole that causes the arc bending of one filament and trapping of another at the same time is shown in Figs. 7(a) and 7(c); the corresponding reconstructions are given in Figs. 7(b) and 7(d), respectively.

More complex configurations of vortex filament trapping, oriented along the x axis, at holes by the looping process, combined by winding with another nearby filament, occurs at a broad spatial scale from 10 μm to 50 μm or more [Fig. 8(a)]. Motion of filaments around the hole occurs in the (x,y) plain, on the melted surface layer. The 3D picture is obtained by tilting the sample table in the SEM between 30° and 60°, depending on the case.

Larger magnification of the local configuration reveals that two vortex filaments, one that makes a loop around a hole and another, bended filament at the rim of the hole become densely winded (and eventually merged), as shown in Fig. 8(b) and in the schematic reconstruction in Fig. 8(c). Similar configuration with rare winding that appear at another location is shown in Figs. 8(d) and 8(e). Very complex organizational stages are reached when splitting of the filament occurs at the touching point with a hole followed by the formation of left-and-right semicircular arcs and their merge into a loop at the opposite side of the hole [Figs. 8(f) and 8(g)].

Interaction of a single vortex filament with a single point defect results in the number of configurations which include arc-bending, formation of loops, rings, splitting of filament in the strain field of a defect, winding, and pinning of filament. These configurations of individual filaments at point defects, establish the first hierarchical level of the vortex filament organization in close interaction with a point defect.

3. Trapping of vortex filament by the spiraling process

A special case of filament organization in the trapping field is the spiraling around point defect shown in Figs. 9(a) and 9(b), generated by 14 pulses of XeCl laser on Co-coated steel. The time between the pulses was 1 s meaning that the sample structure evolves and refreezes in 14 discrete steps. The spiral rotation around a point defect occurs in compression, which makes the filament tip move toward the interior of the defect formed by the bubble explosion. The pattern resembles the stationary form of a vortex filament embedded in a source or sink flow of strength Q (Fukumoto) [11]. Summarizing his results shortly, the filament is wound around a

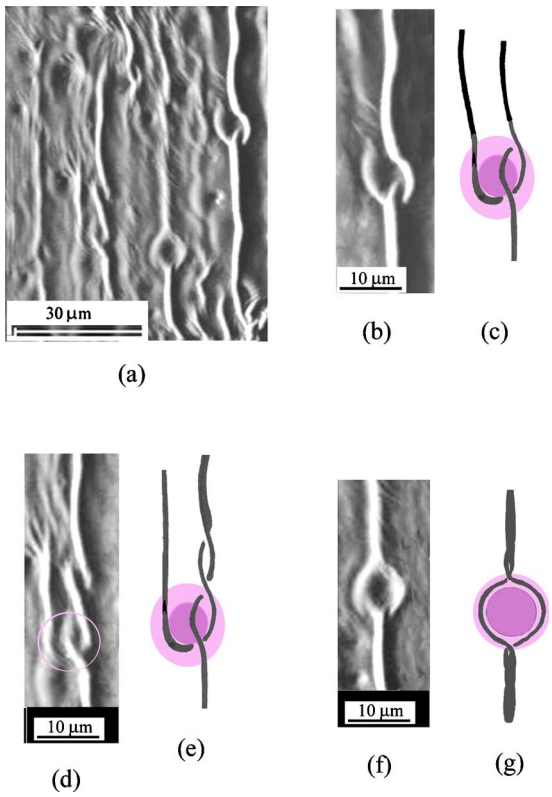

FIG. 8. (Color online) Close interaction of vortex filaments with a hole defect generates a number of configurations (E=86 mJ). (a) SEM micrograph of a complex pattern showing the formation of arcs of various curvature, as well, as of loops. (b) SEM micrograph showing the formation of a loop around a hole. One segment of the filament interacts with another filament that enters a hole and they merge at the exit. (c) Schematic reconstruction of the configuration shown in (b). (d) SEM micrograph showing the formation of a loop around a hole. One segment of the filament interacts with another filament resulting in a helically paired structure. (e) Schematic reconstruction of the configuration shown in (d). (f) SEM micrograph showing the splitting of a vortex filament at the touching point with the hole, together with the formation of semicircular arcs around the hole, and their merge into a single filament on the opposite side. (g) Schematic reconstruction of the configuration shown in (f).

circular cone whose apex angle is determined by the relative strength of vortex with respect to that of the source or sink. Assuming a fluid velocity, V, at the point x [11]:

$$V = \frac{Qx}{4\pi r^3}, \tag{2}$$

with $r=|x|$, while $Q>0$, and $Q<0$, refers to a source or sink flow, respectively. The vector potentials, A, associated with Eq. (2) thought $\mathbf{V}=\boldsymbol{\nabla}\times\mathbf{A}$, can be calculated as [11]

$$A^{\text{source}} = \frac{Q}{4\pi}\frac{(1-\cos\theta)}{r\sin\theta}e_\phi, \tag{3}$$

$$A^{\text{source}} = -\frac{Q}{4\pi}\frac{(1+\cos\theta)}{r\sin\theta}e_\phi. \tag{4}$$

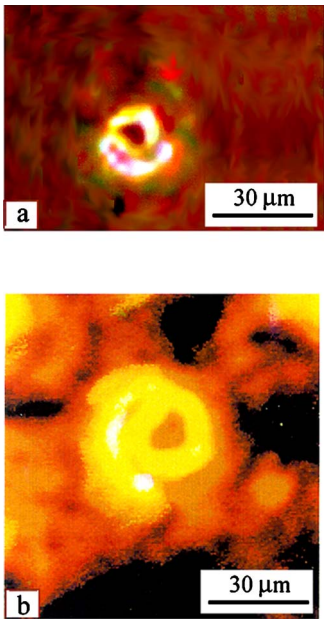

FIG. 9. (Color online) Optical micrographs showing the formation of the spiral pinning of a vortex filament at a point defect, generated by 14 pulses of a XeCl laser on Co-coated steel. Spiral pinning shown in (a) and (b), is very similar (E=250 mJ).

In the presence of the source or the sink flow, vortex filament behaves like a charged particle when it collides to a magnetic monopole. In such cases there exists a constant vector $\mathbf{J}$ defined as [11]

$$\mathbf{J} = \mathbf{X}\times\mathbf{X}' - \frac{Q\mathbf{X}}{4\pi A r}, \tag{5}$$

where $\mathbf{X}=\mathbf{X}(s)$ is a point on the filament curve as a function of arc length s (or on the particle trajectory with s being the time), and the prime ($'$) denotes differentiation with respect to s. The first term of Eq. (5) is the angular momentum of a particle, while the second one describes the total electromagnetic angular momentum. After introducing the polar coordinates (r,θ,φ) using $\mathbf{J}$ as the polar axis, one finds for a trajectory of a charged particle in the magnetic field [11]

$$\left(\frac{r}{d}\right) = \sqrt{\left(\frac{s}{d}\right)^2 + 1}, \tag{6}$$

$$\phi = \frac{1}{\sin\theta}\arctan\left(\frac{s}{d}\right).$$

After elimination of parameter s, Eqs. (6) give

$$\left(\frac{r}{d}\right)\cos(\phi\sin\theta) = 1, \tag{7}$$

where d corresponds to the closest distance the vortex filament–charged particle approaches the sink or source monopole, i.e., at which the origin of parameter, s, was taken.

Since ($\cot\theta=-Q$), i.e., the (charge of the particle) it follows that Q determines the semiangle θ of the cone apex in

3D space, and thus determines the shape of the filament aside from its size which is fixed by d [11]. When projecting the surface of the cone to the plane normal to the cone axis, the cone will transform into a circular Archimedean spiral. Such Archimedean spirals, formed by constant angular velocity ω, are shown in Fig. 9 and described by $R=a\varphi$, with $a \sim 5.5$ μm in Fig. 9(a), and $a \sim 11.25$ μm in Fig. 9(b).

4. Analogy between a vortex filament and an elastic rod

During the resolidification of the LMI melted surface layer, the state of filaments changes from fluid to solid; a three-dimensional configuration of a vortex filament in a fluid crosses over to the Kirchhoff elastic rod; the same configuration is shared by both a vortex filament and an elastic rod (Hasimoto and Kambe [28] and Fukumoto [29]). Accordingly, similar to carbon nanotube looping (Tsukruk *et al.* [15]) the looping of a vortex filament in the field of a point defect can be analyzed on the basis of the elastic rod theory. The mechanism of vortex filament looping could only be valid if the surface tension acting along the shrinking contact line outweighs the strain forces originating from filament bending [15]. The bending properties required for filament folding can be evaluated using the known value of the elastic modulus, ε. The spring constant, K for the portion of a filament participating in continuous bending can be determined, within the limit of the solid rod approximation, by using the equation $K=3\pi R^4\varepsilon/4L^3$, where R is the filament radius and L is the length of the curved portion. Taking into account the size of the loop, and the elastic modulus of the filament make it possible to evaluate the elastic force of the filament and the pinning force, similar to the case of strong looping of carbon nanotubes [15]. The Young's modulus (ε) was found from the standard tabulated values of ε for the materials: 62 GPa (glass), 200 GPa (stainless steel), 0.5 GPa (PTFE), 3.1 GPa (plastic), and 3.0 GPa (paper) and about 1 TPa (carbon nanotubes) (Tsukruk *et al.* [15]), while for double stranded DNA molecule $\varepsilon=0.3$ GPa [30]. The Young's modulus of liquid metal filaments of Pb, Sb, Bi, Au, Ag, Cu, Fe, Sn, Tl, Cd, Co, and Ga, falls in the range between $\varepsilon=1.3\times10^7$ Pa and $\varepsilon=2.2\times10^7$ Pa (Taylor [31]). One therefore finds, that the Young modulus of various metal filaments lies in a narrow interval which makes it possible to estimate the Young modulus of our indium filaments in the same range, i.e., between $\sim10^7$ and 10^8 Pa. Assuming that the radius of the vortex filament, $R \sim 2$ μm, the length of the curved portion, L is between 20 and 40 μm, one finds that the spring constant, K of continuous vortex filament bending ranges from $K \sim 1.3\times10^{-2}$ N/m to $K \sim 2.2\times10^{-2}$ N/m (for $L=40$ μm, $\varepsilon=2.2\times10^7$ Pa) and (for $L=30$ μm, $\varepsilon=1.3\times10^7$ Pa), respectively. Notice that these values for K are comparable to the spring constant of carbon nanotubes ($K \sim 10^{-2}$ N/m), estimated for $L=0.3-1$ μm and $R=1-2.5$ nm (which is well below the critical stiffness of 1–5 N/m required for nanotube bending) [15].

5. Vortex filament stretching caused by the self-induction

Stretching of a vortex filament is the basic mechanism in the trapping process at both solid and hollow spheres.

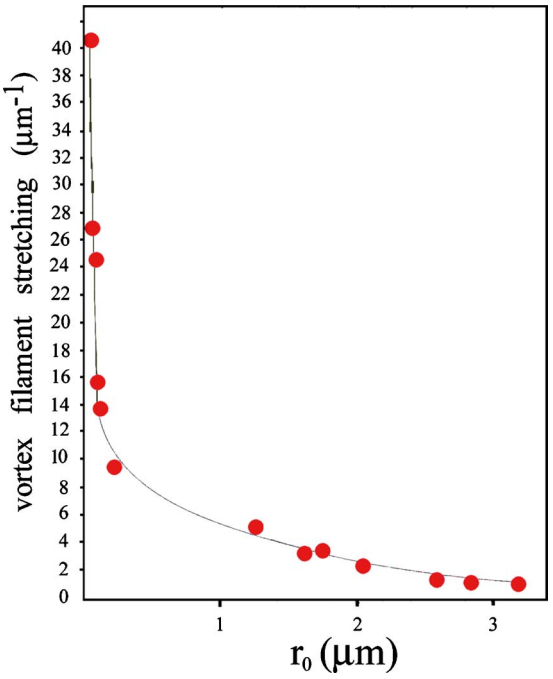

FIG. 10. (Color online) Stretching of vortex filaments as a function of their mean radius r_0. The operating mechanism of vortex trapping at the point defects is self-induction. The strong nonlinear dependence of stretching can be divided into two separated regions, namely at very small, and large r_0.

Stretching enhances vorticity, so, that stretching a vortex filament along its axis will make it rotate faster and decrease its diameter in order to maintain its constant kinetic momentum. More precisely, stretching denoted by γ, is an acceleration of the axial velocity along the vortex ($\gamma=\nabla V$). The vorticity equation is obtained by taking the curl of the Navier-Stokes equation [32]

$$\partial\omega/\partial t + (V\nabla)\omega = (\omega\nabla)V + \nu\Delta\omega, \tag{8}$$

where υ is the kinematic viscosity. The first term represents the time evolution of vorticity, the second is an advection term, the third is the stretching term, and the fourth represents the viscous effects [32]. When stretching is parallel to and points in the same direction as the vorticity, the term $(\omega\nabla)$ is positive and amplifies the vorticity $(\partial\omega/\partial t)$. The vorticity increases and the viscous term $(\upsilon\Delta\omega)$ becomes large enough to counterbalance the amplification term $(\omega\nabla V)$. An equilibrium is reached which imposes the diameter of the vortex filament $\upsilon\omega=\upsilon\omega/r_0^2$. By measuring the mean vortex filament radius r_0 on a series of point defects, the stretching γ was found from $\gamma=\upsilon/r_0^2$ and shown in Fig. 10. Roughly speaking the nonlinear graph in Fig. 10 can be divided into two linear regions: one for the very small filament radius $r_0<1$ μm and another region 1.5 μm$<r_0<3.2$ μm, which seem to be characteristic for LMI.

C. Trapping of a single filament at the random lattice of rigid and hollow spheres

Interaction of individual vortex filament with 2D irregular lattice of bubbles results in more complex configurations

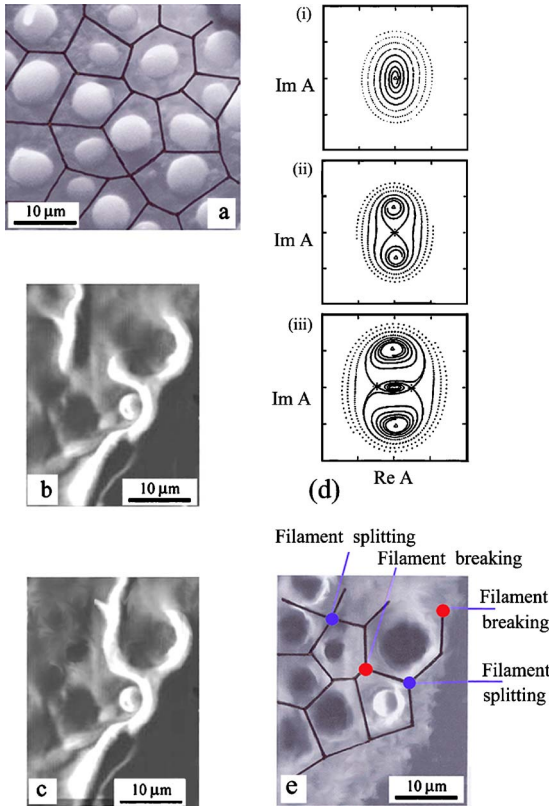

FIG. 11. (Color online) Interaction of a single vortex filament with a 2D random lattice of bubbles (hollow spheres) ($E=86$ mJ). (a) A random bubble system (foam) is represented by the Voronoi lattice (cells). When a vortex filament approaches and touches such a system of bubbles, they explode and form a 2D pattern of holes. (b) The vortex filament first interacts with a rigid sphere and becomes arc-bended; then it interacts with a hole and splits into two filaments. The splitted filament which enters a field of closely packed holes becomes broken, splitted again, etc. (c) We reconstructed the filament configuration before the filament breaks in the strong strain field of the hole defect. (d) Vortex filament splitting occurs at the entrance of the strong strain field of holes that causes core deformation of the holes and can be described by the phase portraits of Eq. (10) (see text). Assuming dissipative perturbation in the deformation field, the vortex filament splitting is obtained for damping coefficient $\delta=-0.1$. (i) $\lambda=-1.5$, (ii) $\lambda=0.1$, and (iii) $\lambda=1.5$ [33]. (e) Construction of the Voronoi lattice of 2D field of holes indicates that the vortex filament splitting and breaking occur at the nodal points of the Voronoi lattice.

which can be analyzed by introducing the corresponding Voronoi lattice of a bubble-foam (crystal), such as shown in Fig. 11(a). Interaction of a vortex filament with a 2D lattice of bubbles causes bubble explosion and initiates a cascade of left and right bending, splitting and breaking of filament, as it can be seen in Fig. 11(b). This picture shows that the vortex filament, during approaching a droplet, is exposed to bending and gets deformed into a semicircular arc. Then, when getting closer to the hole, it is exposed to a large strain field that causes core deformation and induces its splitting into two filaments of smaller diameter [33]. One of the filaments bypasses the hole from the right side, while the left one enters the region between two nearby holes and becomes exposed to an even larger strain field. The strong force exerted by the left hole causes overcritical bending which makes the filament break. Finally, the trapping force of the hole shifts the edge of the broken filament to the left. We reconstruct this process in Fig. 11(c) to illustrate the original (starting) configuration of a vortex filament before breaking. The radius of curvature of the bent portion is smaller than 15 μm (typically between 10 and 20 μm), and may become even smaller. This happens if the hole size is not constant but varies during LMI; the situation is similar to the case of (strong) progressive looping around a droplet as observed for looping of nanotubes during dynamic dewetting [15]. The arc-bended segment of the filament moves towards the hole (or drying droplet) with the radius progressively becoming smaller until it finally becomes a loop.

Splitting of the vortex filament. Figure 11(b) shows that the vortex filament which approaches a hole is exposed to significant local stress which deforms its core and then, either leads to its splitting or breaking. This process can be described by the model of Guckenheimer and Mahalov [33]. Assume that a vortex filament, described in Euclidian space with complex coordinate, A, is exposed to rotation by the group S^1. The vector fields, which are symmetric with respect to this action, can be written as [33]

$$\dot{A} = f(|A^2|)A, \quad \text{with } f:R^+ \to C. \tag{9}$$

If the values of f are purely imaginary the vector field **A** is a Hamiltonian one and the flow is organized into concentric circles, centered at origin. If the flow is damped (due to viscosity), the flow is organized into counter-rotating spirals [33].

Such a damped system, according to the model [33] may have three different phase portraits:

$$\dot{A} = i(\lambda A - |A^2|A - \varepsilon\bar{A}) - \delta A. \tag{10}$$

If the damping coefficient, δ is small compared to the coefficient of the symmetry breaking deformation, ε (core deformation), the bifurcations do not change with varying λ. Originally, there are two pitchfork bifurcations which form two sinks; the saddle separatrices form the boundaries of the basins of attractions of the sinks for $\delta=0.1$ and $\lambda=0.1$ [Fig. 11(d)(ii)]. However, for $\lambda=1.5$ three sinks appear [33] [Fig. 11(d)(iii)]. The vortex filament splitting configuration exemplified in Fig. 11(b) corresponds to Fig. 11(d)(ii) and can also be identified on many other pictures.

Construction of the Voroni lattice for the particular case shown in Fig. 11(b), and *c* reveals that vortex filament splitting and breaking occurs at the nodal points of the Voronoi lattice (vertices of the Voronoi cells) [Fig. 11(e)].

Collective trapping of rare 1D vortex filament lattice at random lattice of hollow spheres: A foam crystal

The interaction of a 1D filament lattice with the foam-crystal breaks the lattice symmetry and causes the formation of left-and-right arc-bended filaments with a high degree of regularity [Fig. 12(a)]. They bypass a hole from both sides and merge with the neighboring filaments at some distance from the hole. A 1D vortex filament lattice is perturbed, yet

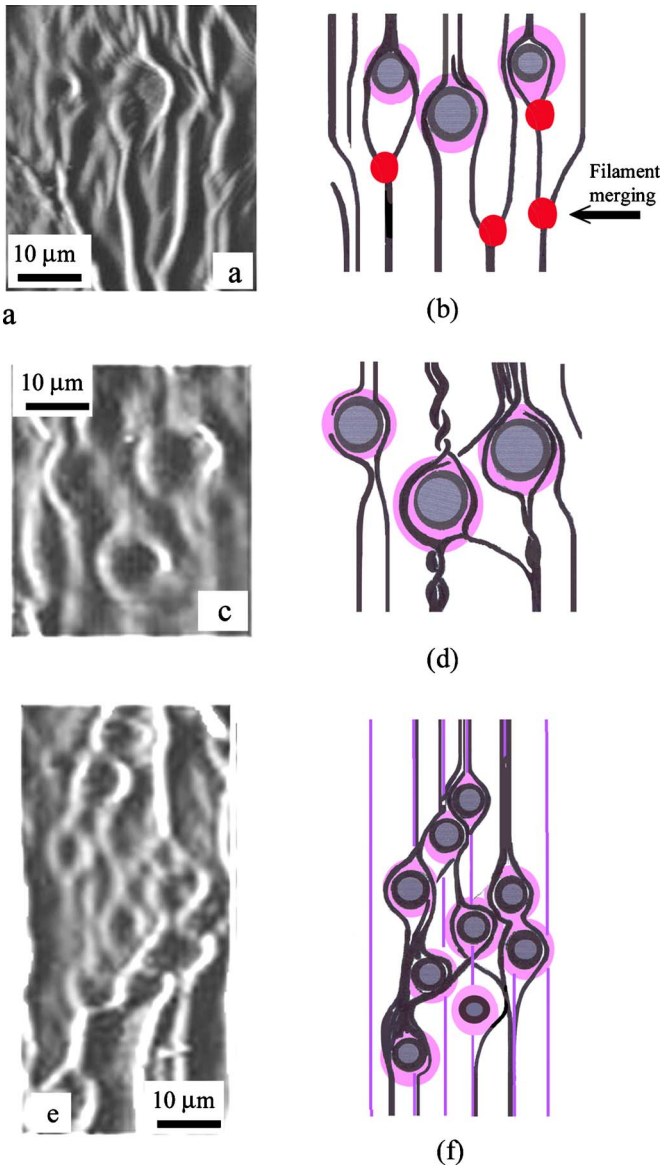

FIG. 12. (Color online) Interaction of a 1D vortex filament lattice with a foam crystal. When a vortex filament touches a soft sphere (bubble) it makes it explode and leads to the formation of a 2D lattice of holes. The close interaction causes the formation of various filament configurations in the field of holes (E=86 mJ). (a) SEM micrograph showing the vortex filament configuration resulting from the interaction of a 1D lattice and random holes. (b) Schematic representation of the configuration shown in (a). (c) SEM micrograph showing semicircular arc bending of filaments and their reconnection into vortex ring. A high hole density of holes prevents looping. (d) Schematic representation of the configuration shown in (c). (e) SEM micrograph showing various arc-bended filaments and their reconnection into vortex rings and knotted structures. (f) Schematic representation of a complex vortex filament configuration corresponding to (e).

filaments keep a certain degree of parallelism. The schematic representation of vortex filament configuration after the interaction of 1D vortex filament lattice and random holes is given in Fig. 12(b). Another type of interaction of 1D vortex filament lattice and random holes in which merging of vortex filaments occurs near the hole, is shown in Fig. 12(c). Notice, that transversal reconnection appears between neighboring filaments. A high hole density prevents the looping process and causes the formation of semicircular arcs as well as their reconnection. Schematic representation of this configuration is given in Fig. 12(d). A more complex configuration of vortex filaments after interaction with 2D random lattice of holes, that exhibits transversal reconnection of filaments and formation of closed loop (ring) structures, is shown in Fig. 12(e). Various arc-bended filaments touch each other and reconnect giving rise to the formation of rings and knotted structures. Corresponding schematic representation of this complex vortex filament configuration is given in Fig. 12(f).

The analysis shows that knotting occurs along the sides of the 2D Voronoi lattice of holes giving rise to the formation of 1D and 2D Hopf-link crystals with typical ring diameter of $\sim$10–15 μm [Figs. 13(a) and 13(b)]. The Hopf link crystals become slightly deformed under the lateral compression caused by the shear. Small-amplitude capillary waves of wavelength $\lambda \sim 1$ to 1.5 μm indicate that reconnection and knotting of filaments and formation of the Hopf-link crystal causes the oscillatory perturbation of the background fluid. Close inspection of the bent vortex filaments reveals that loops are formed by bending only a portion of filaments, typically of, or even less than $\sim 1/5$ of its total length. Buckling was also observed on some bent vortex filaments, indicating nonuniform bending stress distribution over the entire filament, while in other cases uniform thickness was observed indicating uniform distribution of bending stress. Similar phenomena were observed in bending and trapping of strings of carbon nanotubes on silicon substrate [15]. The analogy also extends to carbon nanotube rings and loops organized into 2D random pattern (collection), nanotube buckling, and segmentation [15].

Reconnection of vortex filaments at the sides of the Voronoi cells. The crucial evidence for the formation of Hopf link crystals is the cross-linking or reconnection of vortex filaments which is well supported by the SEM micrograph, shown in Fig. 13(c). The appearance of the heteroclinic streamlines clearly seen in these micrographs is schematically shown in Fig. 13(c) (lower right). SEM analysis of some domains of the Hopf link crystals reveals the reconnection of vortex filaments at certain places where antiparallel vortex filaments are locally deformed and come in close vicinity to each other under an angle. Although these reconnections indicate a topology similar to the Melander-Hussain (MH) model [34] they are more characteristic for the topology of the Zabusky model [35] [Fig. 13(c)]. The MH model assumes antiparallel position of filaments for the numerical simulation and visualization of vortex filament reconnection. In the Zabusky model [35] vortex filaments may start to reconnect moving from any initial position [Fig. 13(d)(i)] into antiparallel one. After the different first step the two models share the following common characteristic phases: [Fig. 13(d)(ii)] *inviscid induction* followed by core flattening and stretching, [Fig. 13(d)(iii)], *bridging* of two vortex filaments by accumulation of annihilated and then cross-linked vortex lines and, finally, [Fig. 13(d)(iv)] *separation of recon-*

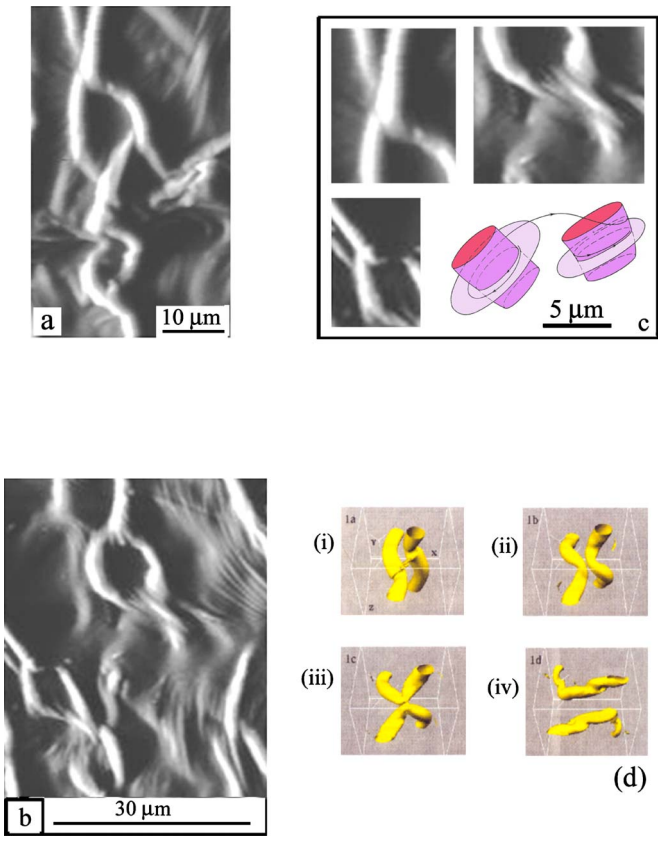

FIG. 13. (Color online) Formation of complex knotted structures as a result of close interaction of a 1D vortex filament lattice with a 2D random lattice of holes (E=73 mJ). (a) SEM micrograph of a chainlike knotted structure of vortex filaments in the field of holes i.e., an example of a 1D Hopf link crystal. (b) SEM micrograph of complex knotted structure of vortex filament lattice in 2D quasiregular field of holes, i.e., an example of a 2D Hopf link crystal. (c) An SEM micrograph evidencing vortex filament reconnection in three different cases observed under different viewing angles. The lower right picture is a schematics drawing of heteroclinic orbits present in reconnection. (d) Numerical simulation and visualization of vortex filament reconnection. (i) The reconnection starts from almost perpendicular position of vortex filaments with small fingers between them. (ii) Strong deformation of cores of both filaments and appearance of "humps" that lead to formation of bridge between them. (iii) Reconnection with annihilation of vorticity from the initial phase. (iv) Vortex filament separation after reconnection [35].

nected filaments associated with threading of the remnants of the initial vortex pair in between the two bridges.

Reconnection starts when the contact between the two vortex filaments is established supposing that they are pressed against each other. This naturally occurs if one vortex filament bypasses the hole from the right, and another one bypasses the neighboring hole from the left, and the two filaments meet at the side of the Voronoi cell. At the very beginning, called phase 1 [34], self-induction, by the large scale movement, brings the two vortex filaments together into almost perpendicular position. They undergo considerable core deformation associated with advection of small filaments between them [Fig. 13(d)(i)–(ii)]. Then, the formation of the head-tail structure of a vortex dipole, takes place, and the two cores move upwards by mutual induction as they collide. In other words, parallel to the deformation (i.e., flattening), the cores also undergo significant stretching which controls the annihilation rate by affecting the vorticity gradient across the contact surface [Fig. 13(d)(iv)] [35].

Phase 2 is characterized by a significant annihilation of vorticity at the contact surface, and by the appearance of two "humps" (in MH terminology) that correspond to two ellipsoids (pancakes) of vorticity (terminology of Zabusky *et al.* [35]) [Fig. 13(d)(iii)]. These two humps, called bridges, formed as the middle parts of the vortex lines in the contact zone are annihilated by viscous cross diffusion, while the unannihilated parts of these vortex lines link up and get realigned and collected into bridges. In this process, the circulation, Γ_z in the (x,y) plane is transferred into the circulation, Γ_x in the (y,z) plain [34,35], which ends the reconnection process. The reconnected vortex filaments are helicalized what is very clearly seen in the upper right micrograph in Fig. 13(c).

In the last phase, phase 3, the instability of the tail of the vortex dipole occurs, together with the separation of filaments which move away from each other by mutual induction and leave the tail behind [34,35] [Fig. 13(d)(iv)]. Thus, finally, the remnants of the original vortex filaments have lost most circulation because of annihilation, yet they survive as distinct, slender vortices, or threads [34], hairpins [35], or remnants of initial fingers [34,35]. It should be noted, that phase 3 has not been observed in any of our micrographs, most likely due to the increasing viscosity that suppresses threading at the end of the laser pulse, in agreement with our previous report [7].

The vortex filament organization, resulting from the close interaction of 1D filament lattice with 2D random lattice of holes, establishes the second hierarchical level of complex structures which ranges from semicircular arcs, loops, vortex rings, the Hopf links to 1D chain of rings, and even to 2D Hopf-linked crystals on 2D Voronoi cells of the foam crystal. While splitting and breaking of filaments (down-grading processes) caused by the local concentration of stress occur at the nodal points, the formation of the Hopf link 1D and 2D crystals (upgrading processes) occur at the sides of the Voronoi cells.

Comparing the elements of the first hierarchical level, i.e., the close interaction of a single filament with a single defect, with the elements of the close interaction of 1D filament lattice with 2D random lattice of defects, one finds that elements of the first hierarchical level, are also present in the second one.

The described process is similar to the process occurring in the world of quantum filaments, which is also described by the crystal and foam models using the Hopf-link invariants and knot operators.

D. Collective trapping of dense 1D vortex filament lattice on a hollow sphere

The interaction of a 1D vortex filament lattice with a single hole causes the collective pinning of filaments. The

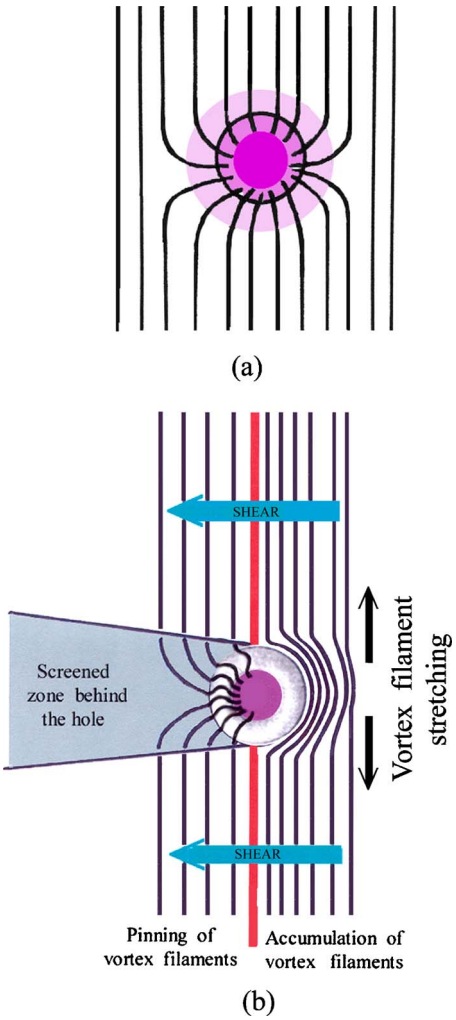

FIG. 14. (Color online) Schematic representation of two types of collective pinning of a 1D vortex filament lattice at a hole. (a) Symmetric pinning at the hole when both the shear and the vortex ring at the hole rim is absent. (b) Asymmetric pinning of a 1D vortex filament lattice at the hole in the presence of shear flow and the vortex ring at the hole rim. The hole represents a discontinuity in the fluid layer so that shear cannot pass over it. In addition, vortex ring represents an obstacle and causes diffraction of the shear wave, which makes a screening zone behind the ring. Vortex filaments accumulate in front of the ring (right), and become pinned in the screened zone under influence of the pinning force of the hole (left).

simplest type of such interaction occurs, when both the shear flow and the vortex ring at the rim of the hole is absent. In this case the collective pinning is symmetric [Fig. 14(a)]. More complex collective pinning occurs in the presence of shear if a dense 1D lattice of filaments interacts with a hole surrounded by a vortex ring at the rim. The shear flow is oriented from the center towards the periphery, i.e., in the counter-gradient direction $(-\nabla T)$, and appears as a symmetry breaking process for collective pinning. Vortex filaments, pushed by the shear flow towards the vortex ring, accumulate and become collectively arc-bended following the curvature of the ring [right-hand side in Fig. 14(b)]. As the hole represents a flow discontinuity shear waves cannot pass it. In addition, the vortex ring represents an obstacle that diffracts shear wave so that a screened zone which is actually a zone of geometric shadow [left-hand side in Fig. 14(b)] is formed behind the hole. In this zone, shear is not present so the vortex filaments can experience the pinning potential, become bended, pass the vortex ring and finally end inside the hole. Depending on the shear strength, two types of collective filament pinning can be distinguished: (a) Weak shear which does not affect the vortex ring. (b) Strong shear which destroys the front of the vortex ring, i.e., the side facing the shear front. Despite the natural variation of features within each type collective pinning, which is due to the locally different conditions in various domains of the spot, the characteristic features observed for week and strong shear are markedly different.

Very weak shear flow. The collective pinning, shown in Fig. 15(a), belongs to weak pinning because the filaments do not take the *S* type double-value-configuration in the circumference of the defect [13]. The symmetry of the 1D filament lattice is broken and those filaments which are in the screened zone, behind the hole, are pinned, while those in the vicinity of the pinning center are only deformed. Under the influence of shear, the vortex filaments at the right-hand side of the pinning center become densely packed and wound around each other because of the transversal perturbation initiated by the oscillatory shock wave. At the left-hand side of the pinning center vortex filament configuration is similar to that on a protrusion as found by Schwarz [12] by numerical simulation of the Biot-Savart law. A vortex filament close to the protrusion reconnects with its image inside the protrusion, whereby the filament is trapped with its leg perpendicular to the surface of the protrusion. Once a filament is pinned, a finite flow velocity is required for its depinning [13].

Weak shear flow. Another collective pinning, similar to the case above, but different in some aspects, is shown in Fig. 15(b). A helical pairing and dense winding of filaments that represent a kind of melted-1D filament lattice are present in the filament accumulation zone [see the right-hand side of Fig. 15(b)]. However, the winding force is much larger than in the above case, indicating strong transversal perturbation of a filament lattice. Perturbation and formation of melted-like filament lattice similar to those in superconductors is caused by transversal periodic perturbation originating from the oscillatory shock wave. Depending on the phase characteristics of the oscillations, the perturbation field can be a coherent or incoherent one. An incoherent transversal perturbation (with random phase variation) causes irregular winding and tangling of the neighboring filaments. Coherent transversal perturbation causes organization of vortex filaments into braided or woven structure [Fig. 15(b)].

Strong shear flow. The collective pinning, shown in Fig. 15(c), exemplifies the strong pining of a 1D filament lattice by two nearby holes. Transversal perturbation causes winding of neighboring filaments and forms structures with an increased, $1.8\times10^4/\mathrm{cm}^2$ filament density. As a result, filaments are organized into a 2D texture due to the complex excitation of the vortex filament lattice which resembles the woven array of nanotubes [15]. caused by complex excitation of a vortex filament lattice. Thus, the rapid process during a nanosecond pulse causes diverse phenomena, such as

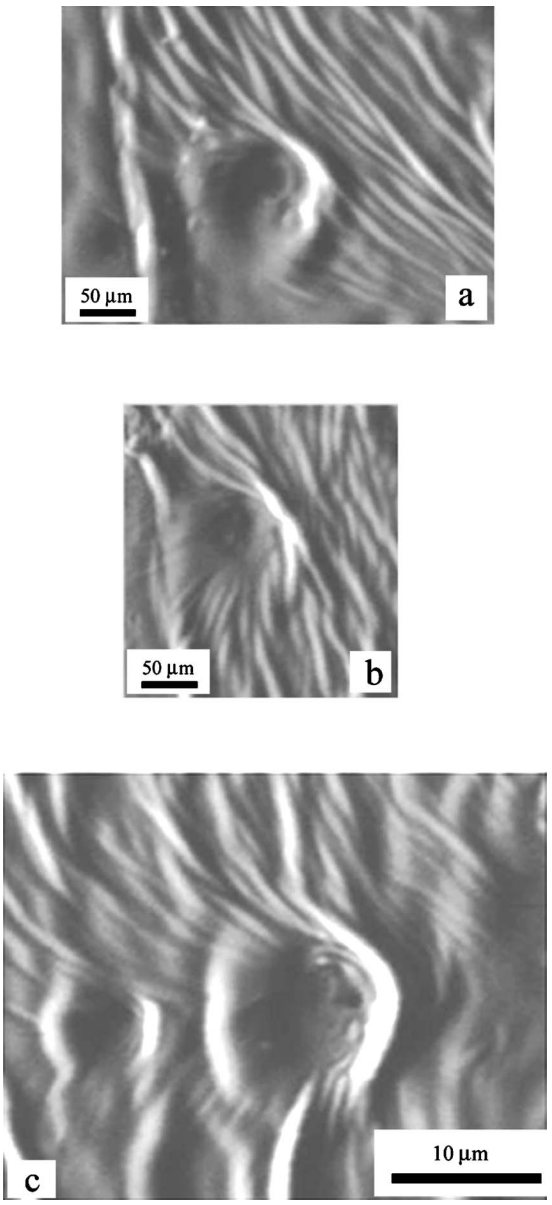

FIG. 15. SEM micrographs of the collective pinning of a 1D vortex filament lattice at a hole with a vortex ring at its rim, in the presence of a shear flow. (a) SEM micrograph of collective configuration of filaments under very week shear showing the accumulation of filaments in front of the vortex ring and pinning in the screened zone behind the ring. Transversal oscillatory perturbation causes winding of vortex filaments in the accumulation zone (right). This collective pinning is a weak pinning, because filaments do not take *S*-type double value configuration inside the hole ($E=86$ mJ). (b) SEM micrograph of collective configuration of filaments in the presence of weak shear showing the accumulation of filaments in the accumulation zone (right) and pinning in the screened zone (right). Strong transversal oscillatory perturbation causes braiding of filaments and formation of a woven texture. (c) SEM micrograph of collective configuration of filaments in the presence of strong shear at two close holes of different size. The large hole has much stronger pinning force which captures those filaments which are in the close vicinity to the small hole.

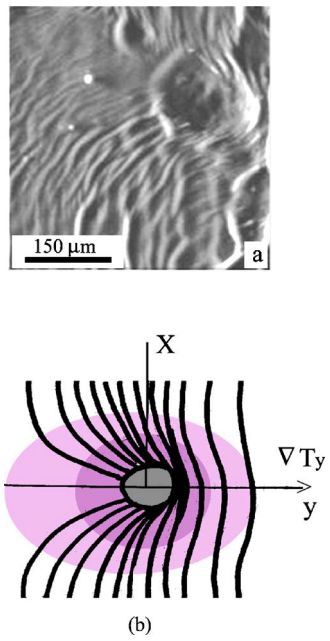

FIG. 16. (Color online) The collective pinning of a 1D vortex filament lattice under the presence of catastrophic shear flow at the hole having a vortex ring at its rim ($E=86$ mJ). (a) SEM micrograph showing the complex pinning of the deformed 1D filament lattice at the hole. Notice that catastrophic shear has broken the vortex ring at the front rim of the hole and caused its elliptical deformation. (b) Schematic presentation of the elliptical trapping field around a hole (the vortex ring is broken and ineffective), with a longer axis oriented along the *y* axis, i.e., in the direction of a shear flow.

intensification of the vortex filaments, their collapse, binding, pulling, core distortion, formation of a complex core, and reconnection in various regions in the vicinity of the hole.

Catastrophic shear flow. The interaction of a 1D vortex filament lattice with a hole in the presence of very strong shear first results, in a catastrophic dynamics which breaks the vortex ring where it faces the shear front. Second, the hole (and the remnants of the ring) becomes elliptically elongated. The elliptical geometry of the trapping force field shown in Fig. 16(a), has a longer axis oriented in the *y* direction (i.e., along the shorter axis of the laser spot), i.e. collinear with the shear. The corresponding schematic representation in Fig. 16(b) shows the elliptical trapping field with the larger perimeter of $\sim 400-500$ μm, and the smaller one of ~ 250 μm, indicating that the pinning (and the deformation) force is ~ 2 times larger in the *y* direction with respect to the *x* one. Interaction between vortex filaments and pinning centers is characterized by a plastic deformation in the vortex system, similar to the one discussed by Blatter *et al.* [13], for pinning of magnetic flux lines in superconductors. Vortex filaments that pass through the regions of larger and smaller compression are exposed to stresses that cause strain resulting in local splitting or merging, which can also be seen in Fig. 16(a). The vortex filament density in the pinning zone, n_f, ranges from $3.8\times 10^4/\mathrm{cm}^2$ to $5\times 10^4/\mathrm{cm}^2$ and is increased by the pressure field caused by the shear flow.

Considering the fluid dynamics inside the hole, two cases are possible; the hole with rotational, or irrotational field. Collective pinning at the hole with the two fields will have different effect on the filament organization inside the hole. In case of an irrotational field merging and stratification will appear, while with a rotational one the vortex filaments will continue to exist inside the hole, being deformed (bended) in the direction of the inner fluid rotation. Although the SEM micrographs are not very clear in this respect, it seems that stratification of filaments inside the hole is seen in Fig. 15(a), while the conservation of slightly bended filaments may be present in Fig. 15(b). The stretching and intensification of vortex tubes in a turbulent flow is believed to be the dominant way in which the energy is distributed, or cascades among the different hierarchical levels. Research has suggested that the interaction of vortex tubes leads to singularities of vorticity in a finite time in inviscid flows and to bursts in viscous flows (Howley and Zabusky [9] and Zabusky *et al.* [36]).

Vortex filament stretching caused by transversal shear flow. The shear flow that breaks the symmetry of a 1D vortex filament lattice and pushes filaments to the vortex ring at the hole's rim, causes their stretching [Fig. 17(a)]. Figure 17(a) shows the dependence of filament core size, σ on the diameter, D of a hole-ring obstacle. Up to $D \sim 120$ μm the core size of the filaments, σ increases with increasing hole diameter (i.e., with decreasing shear strength). However, for a catastrophic shear, i.e., for very large hole diameter $D \sim 132$ μm, the core size suddenly decreases.

Vortex filament pairing caused by transversal shear flow. The period of vortex filament pairing, h in the vicinity of the hole/ring/obstacle, strongly depends on the strength of the transversal shear flow [Fig. 17(b)]. For strong shear flow h is ~ 7 μm; as the shear decreases the period increases in a nonlinear fashion and reaches very high value of $h \sim 170$ μm for very weak shear. For even smaller shears, the period shows singularity, virtually tending to infinity. This practically means that as the shear becomes extremely small, the transversal (oscillatory) perturbation of vortex filaments (which is responsible for their pairing) vanishes. Consequently, the helical period increases and finally becomes larger than the size of the observed domain. However, for very large or the catastrophic shear, the greatest amount of energy is used for breaking the vortex ring, so that transversal perturbation is low again; consequently, the helical period strongly decreases and becomes small again, i.e., reaches $h \sim 10-15$ μm, which is characteristic to a low shear flow.

The filament organization resulting from the close interaction of 1D vortex filament lattice with a hole, establishes the third hierarchical level of the LMI driven complex structures. In the absence of both the shear and a vortex ring at the hole's rim, the structures are characteristic to weak symmetric pinning. When, as the symmetry breaking element, radial shear is present more complex filament organizational stages became obvious for the close interaction of 1D filament lattice with the hole that has a vortex ring at its rim.

The accompanying helical pairing, braiding, or tangling, as well as the formation of woven structures (in the filament accumulation zone), which is caused by the transversal oscillatory shock wave, forms the finer structure in this hierarchical level.

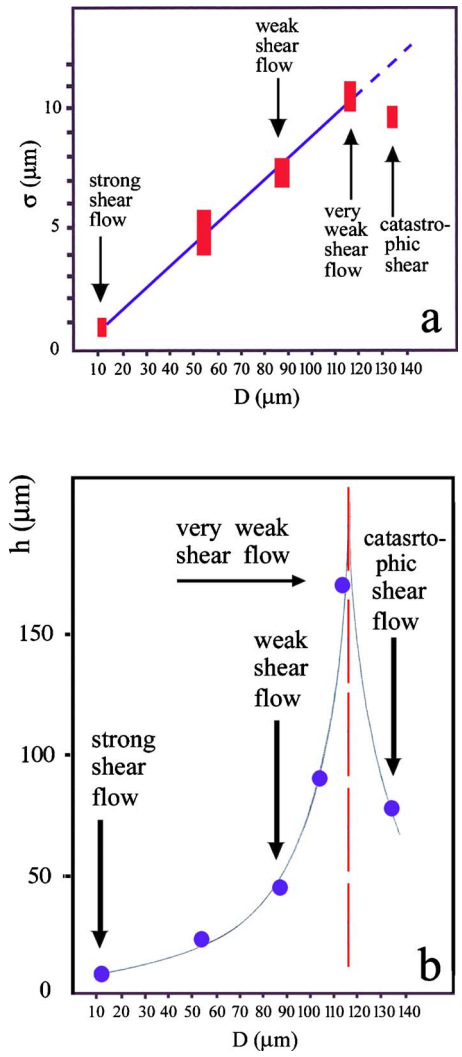

FIG. 17. (Color online) Characteristics of vortex filaments in the presence of a shear flow. (a) The core size of filaments, σ, as a function of the hole diameter, D. The intensity of the shear flow is also marked. (b) The period of helical pairing, h, as a function of the hole diameter, D. The intensity of the shear flow is also marked.

Comparing the elements of the first hierarchical level (i.e., single filament-single defect interaction), the second level (i.e., 1D filament lattice–2D lattice defect interaction) and the third one (i.e., 1D filament lattice–single defect interaction), one finds that the third hierarchical level comprises some elements of the previous two hierarchical levels.

The existence of three hierarchical levels and the fact that some configurations are common in all of them, indicates the presence of a super complexity in the organizational process.

IV. CONCLUSION

The laser-matter interaction on an indium target surface (comprising parallel scratches) in the semiconfined configuration, generates a 1D lattice of parallel filaments along the longer axis of the laser spot that interacts with point defects

like droplets and bubbles. A close interaction with point defects results in a number of configurations of individual filaments and multifilament ensembles, individual and collective pinning with lattice symmetry breaking, reorganization of filaments and other subsequent phenomena at various levels of complexity. Vortex filament organization on a single defect, and a 1D filament lattice with a 2D random lattice of holes includes the looping process predicted by Pedrizzetti [10], the spiraling predicted by Fukumoto [11], and the pinning at protrusions predicted by Schwarz [12].

Close interaction of a vortex filament with point defects gives rise to the formation of structures such as arcs and rings. The interaction of a vortex filament with a 2D random lattice of defects (represented by the corresponding Voronoi lattice), in addition to arcs and rings exhibits filament splitting and breaking which occur at nodal points of the Voronoi cells. On the other hand, the interaction of a 1D vortex filament lattice with a 2D random lattice leads to a series of reconnections resulting in the formation of Hopf links, and 1D and 2D Hopf-link crystals, with the linking established along the sides of the Voroni lattice. We found a reach spectrum of configurations generated by the individual and collective vortex-filament interaction with individual point and 2D lattice defects, which establish not one, but three hierarchical level of gradually increasing complexity. These levels, of which every higher complexity one comprises at least partially the lower complexity one(s), actually indicate the presence of a supercomplexity, a subject that requires further analysis.

This study has provided experimental evidence for the generation of vortex filament configurations resulting from close interaction of individual vortex filaments and 1D vortex filament lattice with point defects. The study shows that dynamics of melted surface flow layer in reality is much more complex than usually assumed, indicating presence of such phenomena in various laser technologies, and as the (the transient phenomena) in laser fusion as well. The study sheds more light on the similarity of phenomena taking place at the *atomic scale* like behavior of vortex filaments in superfluids; on the *microscale* like microfluid dynamics on laser fusion targets, or the behavior of organic polymers and biofluids on natural and artificial (engineered) point defects of their respective substrates, and finally on the *mega* or astrophysical scale as well.

ACKNOWLEDGMENTS

One of the authors (S.L.) would like to express his gratitude to Norman. J. Zabusky, Department of Complex Physics, Weizmann Institute of Sciences, for very inspiring discussion, and suggesting the terms "supercomplexity" and "multiscale phenomena," as well as for his invitations to the Weizmann Institute.

[1] S. Lugomer and A. Maksimović, J. Appl. Phys. **84**, 4684 (1998).
[2] S. Lugomer, J. Appl. Phys. **83**, 510 (1998).
[3] S. Lugomer and A. Maksimović, J. Appl. Phys. **82**, 1374 (1997).
[4] S. Lugomer, Phys. Lett. A **242**, 319 (1998).
[5] S. Lugomer, Phys. Lett. A **259**, 479 (1999).
[6] N. J. Zabusky, S. Lugomer, and S. Zhang, Fluid Dyn. Res. **36**, 291 (2005).
[7] S. Lugomer and N. J. Zabusky, Appl. Phys. Lett. **87**, 204101 (2005); S. Lugomer, Phys. Lett. A **361**, 87 (2007).
[8] N. J. Zabusky, Annu. Rev. Fluid Mech. **31**, 495 (1999).
[9] J. F. Hawley and N. J. Zabusky, Phys. Rev. Lett. **63**, 1241 (1989).
[10] G. Pedrizzetti, J. Fluid Mech. **245**, 701 (1992).
[11] Y. Fukumoto, Proc. R. Soc. London, Ser. A **453**, 1205 (1997).
[12] K. W. Schwarz, Phys. Rev. B **31**, 5782 (1985).
[13] G. Blatter, V. B. Geshkenbein, and J. A. G. Koopmann, Phys. Rev. Lett. **92**, 067009 (2004).
[14] A. Tonomura, H. Kasai. O Kamimura, T. Matsuda, K. Harada. Y., Nayakama, J. Shimoyama, K. Kishio, T. Hanaguri, K. Kitazawa, M. Sasase, and S. Okayasu, Nature (London) **412**, 620 (2001).
[15] V. V. Tsukruk, H. Ko, and S. Peleshanko, Phys. Rev. Lett. **92**, 065502 (2004).
[16] D. Pazo, L. Kramer, A. Pumir, S. Kanani, I. Efimov, and V. Krinsky, Phys. Rev. Lett. **93**, 168303 (2004).
[17] R. A. Ikeda and C. C. Richardson, J. Biol. Chem. **262**, 3790 (1987).
[18] G. M. Whitesides, J. P. Mathias, and C. T. Seto, Science **254**, 1312 (1991).
[19] J. H. Thomas, N. O. Weissl, S. M. Tobias, and N. H. Brummel, Nature (London) **420**, 390 (2002).
[20] E. Priest, Phys. World **16**, 19 (2003).
[21] N. N. Rikalin, A. A. Uglov, I. V. Zyev, and A. N. Kokora, *Laser and e-Beam Processing of Materials* (Mashinostroenie, Moscow, 1985) (in Russian).
[22] J. H. Yo, S. H. Yong, and R. E. Russo, J. Appl. Phys. **88**, 1638 (2000).
[23] A. Miotello and R. Kelly, Appl. Phys. Lett. **67**, 3535 (1995).
[24] Y. Fukumoto and S. Lugomer, Phys. Lett. A **308**, 375 (2003).
[25] S. Lugomer, A. Maksimović, G. Peto, and A. Karacs, Appl. Phys. Lett. **90**, 091917 (2007).
[26] M. R. Dhanak, J. Fluid Mech. **110**, 129 (1981).
[27] M. S. Longuet-Higgins, J. Fluid Mech. **356**, 149 (1998).
[28] H. Hasimoto and T. Kambe, J. Phys. Soc. Jpn. **54**, 5 (1985).
[29] Y. Fukumoto, Fluid Dyn. Res. (to be published).
[30] http://www.uic.edu/classes/phys/phys450/MARKO
[31] G. F. Taylor, Phys. Rev. **23**, 655 (1924).
[32] P. Petitjeans, Europhys. News **34**, 20 (2003).
[33] J. Guckenheimer and A. Mahalov, Phys. Rev. Lett. **68**, 2257 (1992).
[34] M. W. Melander and F. Hussain, Phys. Fluids A **1**, 633 (1989).
[35] N. J. Zabusky, O. N. Boratav, R. B. Pelz, M. Gao, D. Silver, and S. P. Cooper, Phys. Rev. Lett. **67**, 2469 (1991).
[36] N. J. Zabusky, V. F. Fernandez, and D. Silver, Physica D **86**, 1 (1995).